



RESEARCH ARTICLE

Efficient cell classification of mitochondrial images by using deep learning

Muhammad Shahid Iqbal¹ · Saeed El-Ashram^{2,3} · Sajid Hussain⁴ ·
Tamoor Khan⁵ · Shujian Huang² · Rashid Mehmood⁶ · Bin Luo¹

Received: 7 July 2018 / Accepted: 14 December 2018
© The Optical Society of India 2019

Abstract Key challenges for affected cells, evolutionary biology and precision medicine include the effect of drug and understanding viscosity and intensity of drug-treated cells. However, this is extremely difficult because the enormous cells are affected by the drug. We developed a deep learning-based framework DNCIC that can accurately predict normal mitochondria and drug-affected cells that are rare or not observed. For optimization, we used a convolutional neural network and trained using a dataset of mitochondrial images, which were collected through the confocal microscope. The obtained algorithm was validated on the normal and affected cell images. We have trained CNN that can classify (normal and affected cells) two-photon excited fluorescence probe images. The proposed model has classified images and videos with 98%

accuracy. Our results provided a foundation for drug-affected cell diagnosis.

Keywords Cell classification · Mitochondria · Deep learning and drug

Introduction

Medical image diagnosis is very important to recognize whether there exist some diseases or not. To understand medical images, it requires large training and practice, and it is also time-intensive and complex process [1]. DL is a very popular optimization method and is applicable to many fields of science, government and business. One technique for medical image technology is deep learning (DL), specifically using the convolutional neural network (CNN), and it is an edge cutting machine learning technique [2]. In the literature [3–5], it has been shown that the successful learning of hidden patterns of microscopy images improved the image-based diagnosis in pathology, dermatology and radiology, for example, the detection of organ edges in tomography, magnetic resonance image (MRI) and malignant skin lesions, classification of skin lesions [3] and detection of retinopathy [4]. To our best knowledge, DL has not yet been widely applied to detect the drug cell images. Transthoracic echocardiogram (TTE) is a type of echocardiogram, and it provides moving or still images of the internal part of the heart. A TTE consists of images and video clips, Doppler recording measured through different angles, and it offers to balance views of cell images. The main information is acquired through video clips PW (only pulsed wave Doppler), continuous wave (CW) Doppler, and the mode recording is represented exclusively as the single image. In echocardiogram,

✉ Muhammad Shahid Iqbal
nawabishahid@yahoo.com

Bin Luo
luobin@ahu.edu.cn

¹ School of Computer Science and Technology, Anhui University, Hefei, China

² College of Life Science and Engineering, Foshan University, 18 Jiangwan Street, Foshan 528231, Guangdong Province, China

³ Faculty of Science, Kafrelsheikh University, Kafr El Sheikh, Egypt

⁴ School of Applied Sciences and Humanities (NUSASH), National University of Technology, Islamabad, Pakistan

⁵ School of Economic Information Engineering, Southwestern University of Finance and Economics, Chengdu, People's Republic of China

⁶ College of Information Science and Technology, Beijing Normal University, Beijing 100875, China

determining the view is the first step [6]. Some previous methods are time-consuming, and it operates as manual selection features (e.g., tracking of the heart outline), deep learning outperformed in high-dimensional problems, such as image recognition [7–12], DL [13–19], feature-based analysis of histopathological images [20], classification of HEp-2 cell IIF image [21], detection of cancer cells by SVM and RFT [22] and classification of apical echocardiograms [23]. No previous study has investigated the drug cell classification; however, there are a few studies that attempted to classify the drug-treated cells. We classify the drug-treated cells and normal cells, which is a unique contribution toward the effective classification of drug-treated cells and normal cells. We have implemented three different methods: logistic regression, support vector machine (SVM) and convolutional neural network (CNN), and deep learning performs much better than conventional machine learning methods. In deep learning, we have tested CNN, and it automatically classifies drug-treated cells and normal cells, without requiring prior manual feature selection. The proposed model has achieved 98% overall test accuracy, which is based on videos and images. The proposed method achieves traditional impact in medical studies, including tumor. Firstly, the potential method achieves high accuracy with clinical relevance. The relevancy is clearly identified from tumor cell classification that can be used for heat therapy. Therefore, the clear identification of affected cells (tumor cells) helps to diagnose the tumor (heat therapy). Secondly, deep learning techniques are often considered very high amount [24, 25] of data. We sought to achieve high accuracy through minimal data usage. Thirdly, it helps the drug making organizations to check the effect of newly made drug on normal cells, and it also classifies normal and drug-treated cell images. These results suggest that our method may be useful in medical fields, including tumor to check the effect of drug on a specific part of those cells, which improve their accuracy, efficiency and workflow and provide a foundation for high-throughput analysis of drug-treated and normal cell data.

Method

Data set

The images of this compound (TPEF) were taken through confocal microscopy at different time points (1, 12, 24 and 48 h after injection), and it has two types: drug-treated and normal cell images. Total more than 250 images were taken: 142 normal and 138 drug-treated cell images [1]. In Fig. 1a, first four pictures are shown, and each picture is taken after five min. Normal cell images have two types: In

the first type, the images of the whole culture cells were taken, and in the second type, every single cell was taken individually. Figure 1b presents the images of cells either singly or combined after drug injection, and Table 1 shows the detailed description of the data set, which was used for the current experiments.

Method explanation

In this article, we have focused on the method, which can quickly reconstruct drug cell (affected cells) image along with accuracy, and it reduces the computational effort. To achieve high accuracy, we replaced current method for ghost imaging (GI), and it benefits from DL. In this study, we attempted to utilize the benefits of DL to increase the performance of drug-treated cell classification. The main goal of our method is to reconstruct the target image accurately with the low sampling rate and quickly [26]. However, DL has not yet been applied to drug-treated cells. For this network architecture, we have used GoogLeNet-22 network and model utilized small convolutional filters and connected with max pooling layer windows (Fig. 3), and dropout are utilized in training, for both (convolutional and fully connected) layers to prevent overfitting. The overall framework of the proposed method is shown in Fig. 2. Cells were cultured and treated with a drug (n-methyl pyridinium moiety) [1]. Then, cells were posed and convolutional neural network was used to extract features from TPF (two-photon excited fluorescence probe) compound images and mapped them to feature space. Finally, we used a classifier to calculate the probability of each cell and select the highest probability of drug as an auxiliary diagnosis of our model.

Convolutional neural network algorithm

This algorithm was developed by using GoogLeNet with network architecture of twenty-two layers. We have used Caffe deep learning, which is widely employed and the most popular framework. This method used back propagation to train network, and gradient weights can be computed very efficiently, and all layers are fine-tuned through Adam. The global learning rate is 0.0001, and we have resized image 270×270 pixels. Images were compatible with GoogLeNet. In our method, the training CNN system created a probability score for every image ranging from 0 to 100%, which showed the probability of a given image, and its final classification is adopted, with the highest probability. We statistically evaluated whether CNN could recognize cell images (drug-treated cells or normal cells) (Fig. 3), and a brief summary of the study design is shown in Fig. 2. In this neural network algorithm for classification, it included two convolutional layers, two pooling layers and one fully connected layer. The node is

Fig. 1 Two-photon excited fluorescence probe images data sets: **a** normal cells images, cells were cultured and then the images of these culture cells under normal condition were taken by using confocal microscopy; **b** drug-treated cells images; some drugs are added to the normal cells, and the images of affected cell were taken and the viscosity and variation were checked

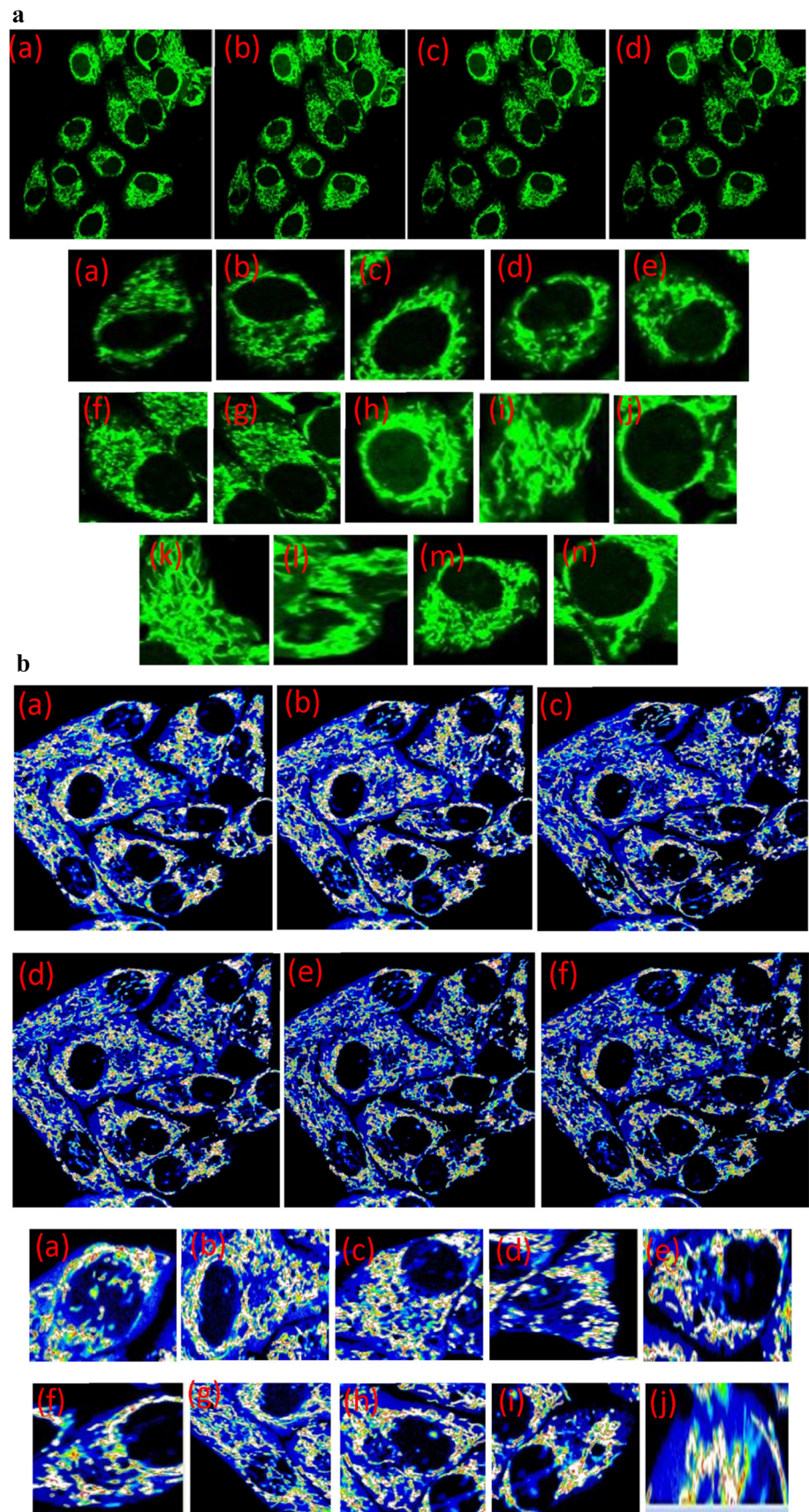


Table 1 Real-time images (TPEF probes)

Image types	Number of images
<i>Data description (TPEF) probes</i>	
Normal	142
Drug treated	138

1028 and 512. The Softmax classifier consists of 15 nodes, and it depends on the classification tasks, such as the convolutional layer (CL), max pool (max pooling layer) and fully connected layer (FC) (Fig. 3). In Fig. 2, convolution neural network for image classification is shown, and ramp function was added to serve as an activation function between the first convolutional layer and the pooling layer, also between the second convolutional layer and the pooling layer, as well as between the second pooling layer and the last linear layer. The total images (normal, 148 and drug, 138, $m = \text{normal}$, $n = \text{drug}$) were taken as input, data were split as training (normal, drug), test set (normal, drug), and classified cell images were predicted (Fig. 4). Training, validation and test data were split by study, and test data were not used for training or validating the model.

The model was trained to classify images, with video classification as majority rules vote on related image frames. Figure 3 shows the CNN for drug cell classification. Initial step image input data were obtained by subtracting the mean value (see Eqs. 1 and 2).

$$\mu = \left(\frac{1}{M} \right) \sum_{k=1}^M x_k \quad (1)$$

$$x'_k = x_k - \mu \quad (2)$$

The normalized image patches are x_k , and M is the total number of image patches. For decomposition of the eigenvalue, it is computed through covariance matrix (see Eq. 3). M is total image patches samples from the dataset, and eigenvectors are denoted as $u_1, u_2, u_3, \dots, u_n$, and corresponding eigenvalues $\lambda_1, \lambda_2, \lambda_3, \dots, \lambda_n$ then computed the covariance matrix.

$$\sum = E(xx^T) = \frac{1}{M} \sum_{k=1}^M (x'_k)(x'_k)^T \quad (3)$$

In convolutional layers, the output feature map in layer 1 is shown in Eq. 4. The convolutional operation is denoted

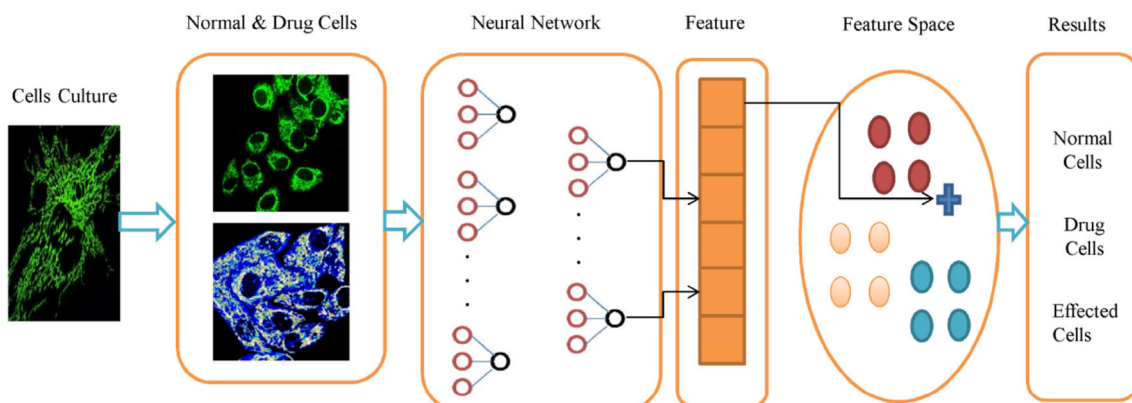


Fig. 2 The proposed framework (DNCIC): the cells are cultured and drug was added to the cells, the pictures of culture cells were taken (normal and affected cell images) with CNN application, features were extracted, and images were classified

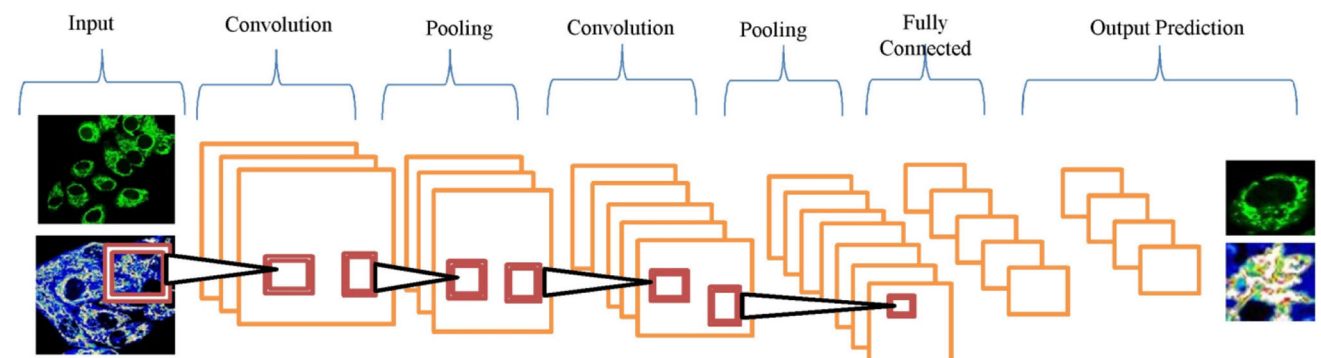
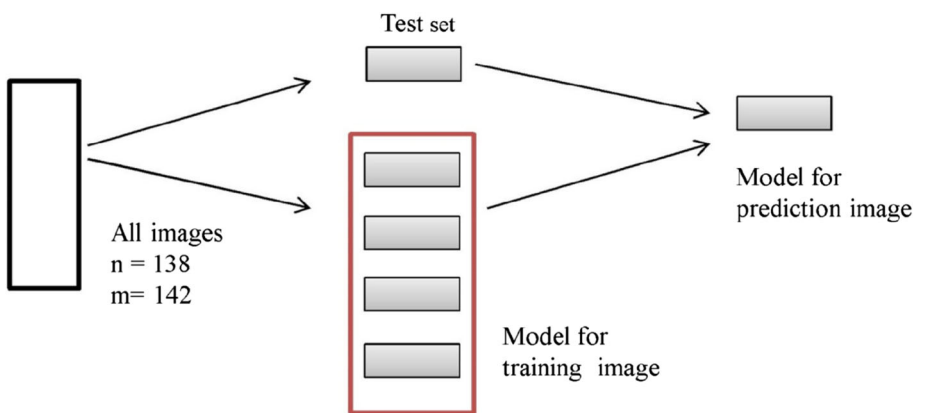


Fig. 3 Convolution neural network for image classification, two types of images, drug-treated and normal as an input, two convolution layers, two pooling layers, max pooling, one fully connected layer, and the output prediction: normal and drug-treated images

Fig. 4 Convolution neural network (CNNs) for drug cell classification, for all images, $m = 142$, normal cell image, and $n = 138$ drug-treated cell images, and the model was trained by using drug-treated and normal images and then tested and classified as normal and affected cells. training 70% and test 30%



as $*$, and f is nonlinear mapping sigmoid, and it is defined as $f(x) = 1/(1 + e^{-x})$. W_{mn}^l is the weighting filter and randomly initialized at the start and then trained with the BP algorithm and optimized with SGD (stochastic gradient descent).

$$x_n^l = f \left(\sum_m x_m^{l-1} * W_{mn}^l + b_n^l \right) \quad (4)$$

In fully connected layer, binary classifier is used, and logistic regression (LR) in Eq. 5 is formulated as y denotes a class label, $x \in K$ -dimensional feature vector, and $w \in$ the weight parameter. The output probability is shown in Eq. 6, $w = [w_1, w_2, \dots, w_n] \in R^{(K+1) \times N}$ and each w represents the weight parameter of that class.

$$P(y = 1/x; w) = \frac{1}{1 + \exp(-w^T x)} \quad (5)$$

$$P(y = 1/x; w) = \frac{\exp(w_i^T x)}{\sum_{i=1}^N \exp(w_i^T x)} \quad (6)$$

In the optimization method, SGD implementation updates weight parameter in each iteration. It can help scale the large dataset with satisfactory results [11]. Therefore, the gradient parameters are computed mini-batch training examples, and new update iteration is shown in Eq. 7. The learning rate is denoted by α , and the update parameters are calculating the cost and gradient by the mini-batch size of a training set. The γ is used as a fraction of the update vector (see Eq. 8).

$$W_{i+1} = W_i - \alpha \nabla w_i E(W) \quad (7)$$

$$v_i = \gamma v_{i-1} + \alpha \nabla w_{i-1} E(W) \quad (8)$$

$$W_{i+1} = W_i - v_i \quad (9)$$

V_i is the velocity vector, and W is the parameter of a vector. For the learning stability, γ is set as 0.0001 learning rate. The evaluation method used several evaluation indicators, which are commonly used in the classification task to

evaluate the performance of our model. Their conceptions and formulas are described as follows:

Accuracy

$$= \frac{(\text{True Positive}) + (\text{True Negative})}{(\text{True Positive}) + (\text{False Positive}) + (\text{False Negative}) + (\text{True Negative})}$$

where true positive (TP) means a trend is up, and it is classified as up. The true negative (TN) means a trend is down, and it is classified as down. False positive (FP) means a trend is down, but it is classified as up. False negative (FN) means a trend is up, but it is classified as down.

Results

In this article, mitochondrial images are the quantitative measure of drug-treated and normal cells, and it can be identified as expected tumor cells and helpful for medical diagnosis based on biological compound image data. State-of-the-art for mitochondria affected drug cell image, and it takes advantages of a strong association with medicine as well as tumor variable with drug images. Deep learning achieves very high-level classifications, such as drug-treated and normal cell images and trained convolutional neural network (Fig. 3).

Newly developed CNN method for mitochondrial cell images with high accuracy

First, the images were categorized into two types: normal and drug-treated cell images. Our newly developed CNN classified images correctly with 98% accuracy (Table 2). We have trained CNN model, with two convolution layers and two dense layers (see the Discussion section) for details of CNN architecture (Fig. 3). We have implemented three different methods, such as LR, SVM and CNN. The proposed model DNCIC (Fig. 2) recognized the drug-treated and normal cell images. For the training of model,

Table 2 Results of different methods, where “CNNs” indicates the performance of the proposed model

Methods	Data types	Accuracy
<i>Predicted accuracy of drug-treated and normal images</i>		
LR	Normal/drug images	0.56
SVM	Normal/drug images	0.65
CNNs	Normal/drug images	0.98

we used pre-train GoogLeNet, and the dataset of training images consisted of 300 images (Fig. 1a) and the test dataset consisted of 150 images (Fig. 1b). The accuracy of the model is 98.23% (Table 2). We have used the stochastic gradient descent (SGD) with momentum 0.9 to train parameters of our network. Therefore, our model very quickly converges during the training processing. Training after about 4 epochs, our model attained 95% accuracy and one simple CPU (Fig. 5a). One epoch means it completed one session (all training simples) and can reach high accuracy, and loss curve becomes smooth, which can be seen in Fig. 4a and after 10 epochs (Fig. 5b). When 100 epochs were applied, our model attained 98% accuracy% (Fig. 5c). From Table 2, we can see the prediction time of each drug-treated and normal cell images, which is between 10 and 20 ms, and it can be predicted in real time (CPU). Table 2 shows the accuracy of the three machine learning methods; LR, SVM and our proposed model (CNN) are reported. These three machine learning methods, which we have compared and applied on two-photon excited fluorescence probe images, achieved more accurate results (Table 1). We can see that our proposed model has achieved the best results as compared to the other methods, and on the test set our method achieves 98% accuracy and recall rate of 96%, which strongly prove that CNN does have the strongest capability compared to the other algorithms (Fig. 7). Table 3 shows an average prediction time of our method for each drug image (two-photon excited fluorescence probes), for each test set, and we can observe that our model execution time of one epoch is only 13.83 ms, which indicates that our method is very efficient in the diagnosis process. Our model can automatically extract high-level semantic features from drug-treated and normal cell images and map them to a high-dimensional feature space (usually hundreds to thousands of dimensions). We already mentioned that we can use t-SNE (distributed stochastic neighbor embedding) 39 and 40 techniques for higher-dimensional feature. In feature space, each point represents drug-treated cells and each color represents drug-treated or normal cells. In the first epoch = 0, model parameters are randomly initialized, all drug-treated and normal cells in the feature space are

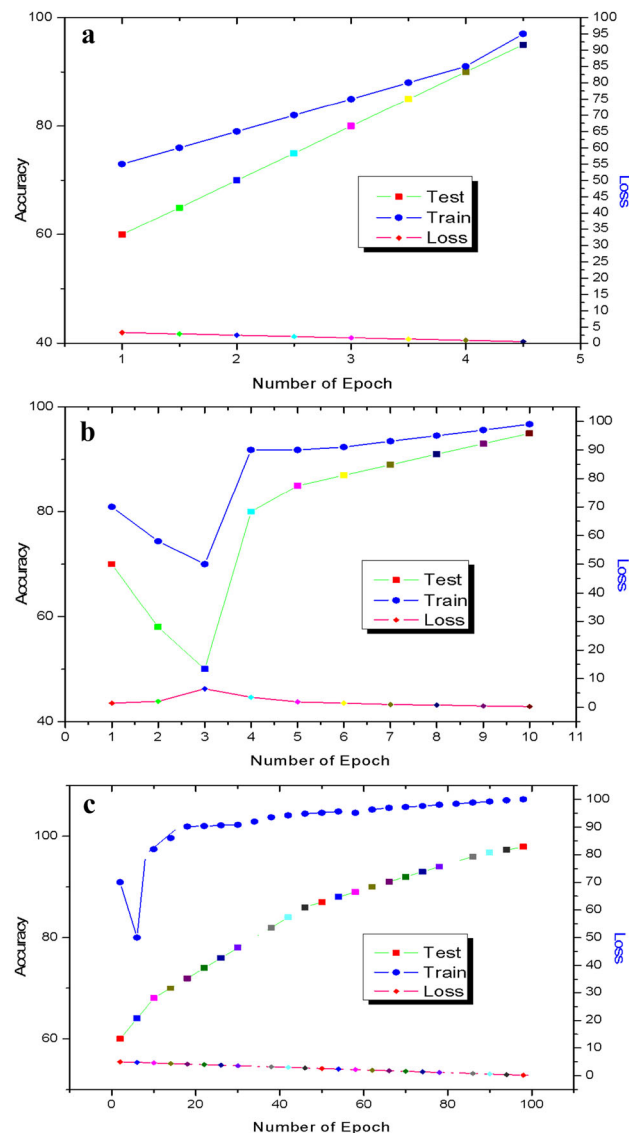


Fig. 5 The process of training and results: **a** train/test accuracy and loss with the 4 epochs show the training, test and loss under 4 epochs, and our approach, with accuracy 0.95%, **b** train/test accuracy and loss with the 10 epochs show the training, test and loss under 10 epochs, and our approach, with accuracy 0.96%, and **c** train/test accuracy and loss with the 100 epochs show the training, test and loss under 100 epochs, and our approach, with accuracy 0.98.23%

Table 3 Results of training time of CNN method

Methods	Epochs	CPU (ms)
<i>Training time of different epochs</i>		
CNNs	4	3
CNNs	10	7
CNNs	100	17

randomly distributed and indivisible, and after 4 epochs, images began separation (Fig. 5a). After 10 epochs, image separation is more clearly identified. When training for 100 epochs, we can clearly see that samples of each normal and drug-treated cell image (Fig. 6a) and completely separated normal and drug-treated cells, the same type of cells becomes cluster together. Figure 5 shows the epoch results,

the process of training, test and loss, and the model achieved 98% accuracy, on 4 epochs 95% accuracy (Fig. 5a), 96% accuracy on 10 epochs (Fig. 5b) and 98.23% accuracy on 100 epochs (Fig. 5c). The classification of the test on the standard laptop takes the average time of 1.1 ms per image.

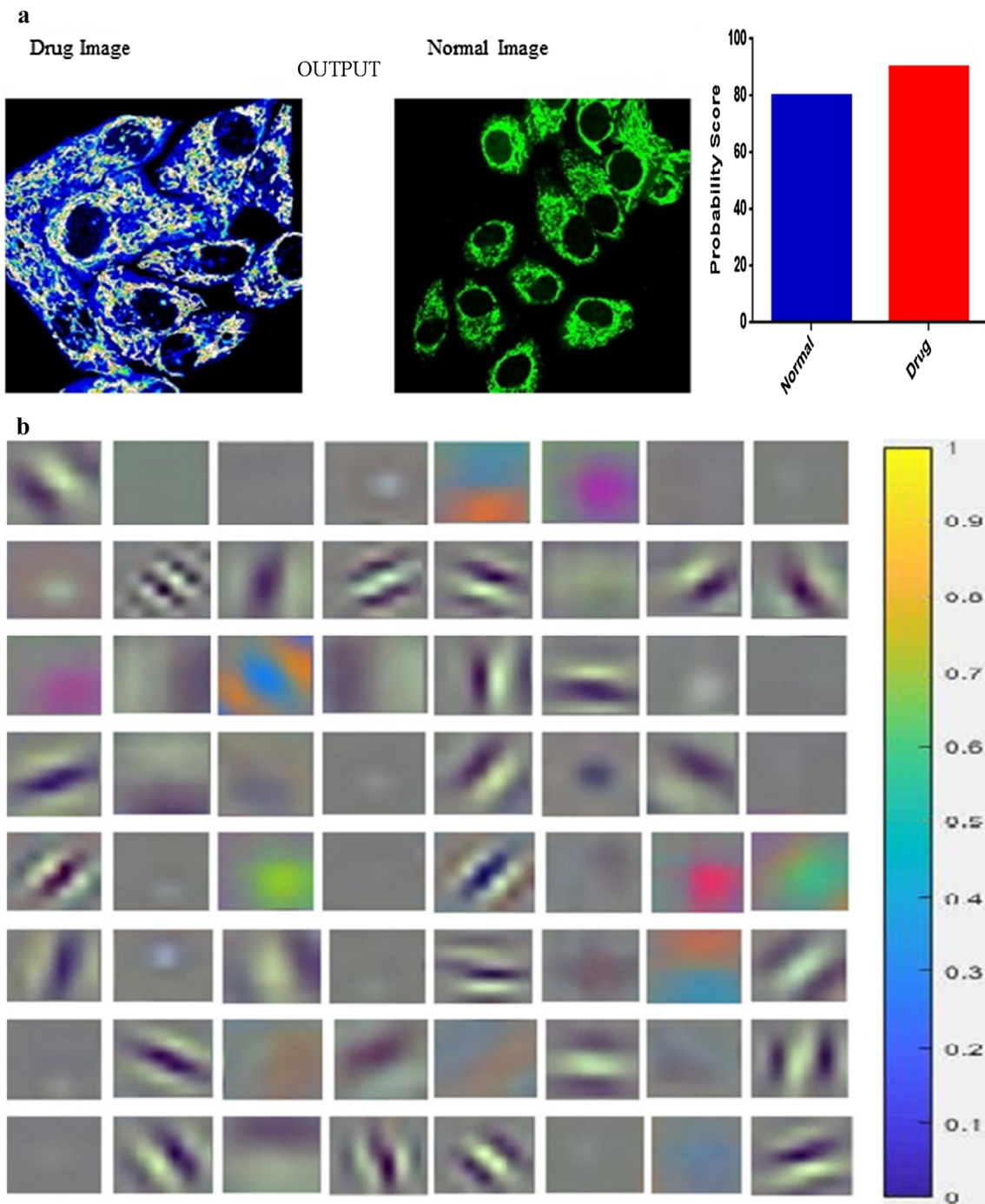


Fig. 6 **a** CNNs correctly classify normal and drug-treated cell images, and the prediction probability of drug-treated and normal images is 80 and 90%. **b** First convolutional layer weights, CNNs share weights in convolutional layers, which means the same filter

The CNN correctly classified mitochondrial images of the drug-treated and normal cells (drug and normal images)

We were curious as to whether CNN could correctly recognize the anatomical location of images acquired from different parts of drug-treated and normal cells. Validation set featured a total of 138 drug images, including 142 normal images. CNN recognized the anatomical location of these cells images accurately with values of 0.98% for drug-treated cell images and normal cell images, as shown in Fig. 6a, and Fig. 5d shows output images. Figure 4e shows first convolutional layer weights. Characterization grid-like representation and spatial plots of linear units in agent exhibit spatial patterns to grid border and place cells are displayed in Fig. 6b.

Discussion

In the past decades, CAD (computer-aided diagnosis) has been an active area of research [27], and it started with the detection of breast cancer on mammograms [28]. A computer-aided diagnosis has been extended to several other diseases, such as colon cancer [29], lung cancer [30] and brain disorder diseases [31]. Only breast imaging was adopted in clinical practice, and its effectiveness was controversial in some cases [32] with unclear accuracy [33]. The important thing is that most clinical computer-aided diagnosis systems are not based on DL, and they used traditional computer vision techniques. DL technique has proven to be effective in many fields, such as object detection; it outperforms traditional techniques [34]. Interest in DL has been increased in recent years [35]. Though, DL has been recently applied for the detection of diabetic retinopathy on retinal photographs [36], skin cancer [37], pulmonary nodule [38] and cerebral microbleeds detection form MR image [39]. In the proposed method, drug-treated and normal cell image classification (DNCIC) is based on DL and simply affects tumor. In our study, we attempted to minimize the difference between predicted drug cells and original drug images. Therefore, our calculations show that loss of drug-treated and normal cells can be aggravated if even there are more powerful machine learning tools, such as DL method, and it makes nonlinear relations between features and produce more accurate results. A tumor is one of most significant health risk factors. In this study, tumor can be diagnosed with heat therapy using unsupervised DNCIC method. The DL method significantly separates between the normal and affected cells, as well as healthy and diseased patients. We implemented three methods (SVM, LR and CNN); however, our proposed method (CNN) has more diagnostic

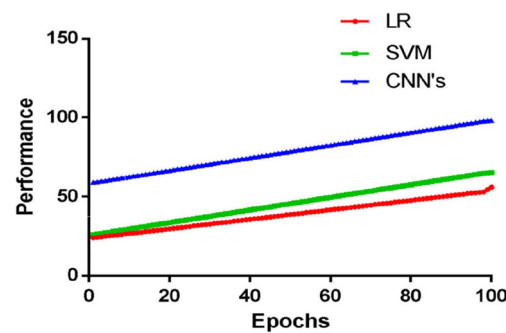


Fig. 7 Implementation of three different methods, including LR, SVM and CNN with 56%, 65% and 98% accuracies

accuracy in comparison with the other methods (Fig. 7). Our findings highlight the power and practical utility of semi-analytic approaches, combining the drug with most powerful modern machine learning tools. This synthesis will eventually produce even better health risks models for tumor, to mitigate longevity risks in medicine, help in pension planning, and contribute to upcoming clinical trials and future deployment of tumor therapies.

Conclusion

In this study, we propose a method for drug-treated and normal cells classification, and this method is useful for the drug treatment as well as tumor identification. In the medical field, when new drugs are made by medical organizations, drugs can be evaluated by using our current method. Medical companies can culture cells and inject the new made drug into these culture cells. After that, they take images of cultured cells, analyze these images and can be identified as normal and drug-treated cells. In tumor diagnosis, nowadays heat therapy becomes popular, and through this method, we can clearly classify the position of affected cells (tumor cells) and treated tumor cells by heat therapy. We implemented three different methods: LR, SVM and CNN, and these methods achieve 56%, 65% and 98% accuracies, respectively. Moreover, the CNN method described here provides an alternative way to the baseline methods, such as LR, SVM.

Acknowledgements The authors are grateful to the School of Computer Sciences, Anhui University Hefei, China, for their support and cooperation.

Author contributions MSI, SEA, SH, TK, RM and BL developed the model and analyzed the data. SH analyzed the data, made new compounds and provided the dataset of normal and drug images. All authors read and approved the final version of the manuscript.

References

1. X. Tian et al., A series of water-soluble pyridinium derivatives with two-photon absorption in the near infrared region for mitochondria targeting under stimulated emission depletion (STED) nanoscopy. *Dyes Pigments Int. J.* **147**, 90–98 (2017). <https://doi.org/10.1016/j.dyepig.2017.07.025>
2. A. Karpathy et al., *The Unreasonable Effectiveness of Recurrent Neural Networks*. github. <http://karpathygithub.io/2015/05/21/rnn-effectiveness> (2015)
3. A. Esteva et al., Dermatologist-level classification of skin cancer with deep neural networks. *Nature* **542**(7639), 115 (2017). <https://doi.org/10.1038/nature21056>
4. V. Gulshan et al., Development and validation of a deep learning algorithm for detection of diabetic retinopathy in retinal fundus photographs. *Jama* **22**, 2402–2410 (2016). <https://doi.org/10.1001/jama.2016.17216>
5. G. Litjens et al., A survey on deep learning in medical image analysis. *Med. Image Anal.* **42**, 60–88 (2017). <https://doi.org/10.1016/j.media.2017.07.005>
6. G. Wharton et al., A minimum dataset for a standard adult transthoracic echocardiogram:a guideline protocol from the British Society of Echocardiography. *Echo Res. Pract.* **2**, G9–G24 (2015). <https://doi.org/10.1530/ERP-14-0079>
7. H. Khamis et al., Automatic apical view classification of echocardiograms using a discriminative learning dictionary. *Med. Image Anal.* **36**, 15–21 (2017). <https://doi.org/10.1016/j.media.2016.10.007>
8. C. Knackstedt et al., Fully automated versus standard tracking of left ventricular ejection fraction and longitudinal strain: the FAST-EFs multicenter study. *J. Am. Coll. Cardiol.* **66**, 1456–1466 (2015). <https://doi.org/10.1016/j.jacc.2015.07.052>
9. S. Narula et al., Machine-learning algorithms to automate morphological and functional assessments in 2D echocardiography. *J. Am. Coll. Cardiol.* **68**, 2287–2295 (2016). <https://doi.org/10.1016/j.jacc.2016.08.062>
10. J. Park et al., fast and automatic Doppler gate localization in B-mode echocardiogram. *Med. Image Comput. Comput. Assist. Interv.* **11**, 230–237 (2008). https://doi.org/10.1007/978-3-540-85990-1_28
11. P.P. Sengupta et al., Cognitive machine-learning algorithm for cardiac imaging: a pilot study for differentiating constrictive pericarditis from restrictive cardiomyopathy. *Circ. Cardiovasc. Imaging* **9**, 1–3 (2016). <https://doi.org/10.1161/CIRCIMAGING.115.004330>
12. A. Madani et al., Fast and accurate view classification of echocardiograms using deep learning. *NPJ Dig. Med.* **1**(1), 6 (2018). <https://doi.org/10.1038/s41746-017-0013-1>
13. D.E. Goldberg, Genetic algorithms in search. *Optim. Mach. Learn.* **7**, 2104–2116 (1990)
14. G.E. Hinton et al., A fast learning algorithm for deep belief nets. *Neural Comput.* **18**, 1527 (2006). <https://doi.org/10.1162/neco.2006.18.7.1527>
15. Matthias Seeger, Gaussian processes for machine learning. *Int. J. Neural Syst.* **14**, 69–106 (2004). <https://doi.org/10.1142/S0129065704001899>
16. Y. LeCun et al., Deep learning. *Nature* **521**, 436–444 (2015). <https://doi.org/10.1038/nature14539>
17. A.E. Brown et al., A dictionary of behavioral motifs reveals clusters of genes affecting *caenorhabditis elegans* locomotion. *Proc. Natl. Acad. Sci.* **110**, 791–796 (2013). <https://doi.org/10.1073/pnas.1211447110>
18. F.J. Ordóñez, D. Roggen, Deep convolutional and lstm recurrent neural networks for multimodal wearable activity recognition. *Sensors* **16**, 115 (2016). <https://doi.org/10.3390/s16010115>
19. Y. Guan, T. Ploetz, *Ensembles of Deep LSTM Learners for Activity Recognition Using Wearables*. arXiv:1703.09370, <https://doi.org/10.1145/3090076> (2017)
20. P. Wang et al., Feature-based analysis of cell nuclei structure for classification of histopathological images. *Digit. Signal Proc.* **78**, 152–162 (2018). <https://doi.org/10.1016/j.dsp.2018.03.008>
21. D. Cascio et al., A multi-process system for HEp-2 cells classification based on SVM. *Pattern Recogn. Lett.* **82**, 56–63 (2016). <https://doi.org/10.1016/j.patrec.2016.03.024>
22. M.R. Hasan et al., Classification of cancer cells using computational analysis of dynamic morphology. *Comput. Methods Programs Biomed.* **156**, 105–112 (2018). <https://doi.org/10.1016/j.cmpb.2017.12.003>
23. H. Khamis et al., Automatic apical view classification of echocardiograms using a discriminative learning dictionary. *Med. Image Anal.* **36**, 15–21 (2017). <https://doi.org/10.1016/j.media.2016.10.007>
24. A. Janowczyk, A. Basavanhally, A. Madabhushi, Stain normalization using sparse autoencoders (STANOSA): application to digital pathology. *Comput. Med. Imaging Graph.* **57**, 50–61 (2017)
25. A. Sethi, L. Sha, A.R. Vahadane, R.J. Deaton, N. Kumar, V. Macias, P.H. Gann, Empirical comparison of color normalization methods for epithelial-stromal classification in h and e images. *J. Pathol. Inf.* **7**, 17 (2016). <https://doi.org/10.4103/2153-3539.179984>
26. P.S. Douglas et al., ACCF/ASE/AHA/ASNC/HFSA/HRS/SCAI/SCCM/SCCT/SCMR 2011 appropriate use criteria for echocardiography. *J. Am. Coll. Cardiol.* **57**(9), 1126–1166 (2011). <https://doi.org/10.1016/j.jacc.2010.11.002>
27. K. Doi, Computer-aided diagnosis in medical imaging: historical review, current status and future potential. *Comput. Med. Imaging Graph.* **31**, 198–211 (2007). <https://doi.org/10.1016/j.compmedimag.2007.02.002>
28. F. Winsberg et al., Detection of radiographic abnormalities in mammograms by means of optical scanning and computer analysis I. *Radiology* **89**, 211–215 (1967). <https://doi.org/10.1148/89.2.211>
29. H. Yoshida et al., Computerized detection of colonic polyps at ct colonography on the basis of volumetric features. *Radiology* **222**, 327–336 (2002). <https://doi.org/10.1148/radiol.2222010506>
30. L. Monnier-Cholley et al., Computer-aided diagnosis for detection of interstitial opacities on chest radiographs. *AJR Am. J. Roentgenol.* **171**, 1651–1656 (1998). <https://doi.org/10.2214/ajr.171.6.9843307>
31. M.R. Arbabshirani et al., Single subject prediction of brain disorders in neuroimaging: promises and pitfalls. *Neuroimage* **145**, 137–165 (2016). <https://doi.org/10.1016/j.neuroimage.2016.02.079>
32. T. Freer et al., Screening mammography with computer-aided detection: prospective study of 12,860 patients in a community breast center 1. *Radiology* **220**, 781–786 (2001). <https://doi.org/10.1148/radiol.2203001282>
33. J.J. Fenton et al., Influence of computer-aided detection on performance of screening mammography. *N. Engl. J. Med.* **356**, 1399–1409 (2007). <https://doi.org/10.1056/NEJMoa066099>
34. K. He et al., Delving deep into rectifiers: surpassing human level performance on imagenet classification, in *Proceedings of the IEEE International Conference on Computer Vision* (IEEE Computer Society, Washington, 2015), pp. 1026–1034
35. H. Greenspan et al., Guest editorial deep learning in medical imaging: overview and future promise of an exciting new technique. *IEEE Trans. Med. Imaging* **35**, 1153–1159 (2016). <https://doi.org/10.1109/TMI.2016.2553401>
36. V. Gulshan et al., Development and validation of a deep learning algorithm for detection of diabetic retinopathy in retinal fundus

- photographs. *JAMA* **316**, 2402–2410 (2016). <https://doi.org/10.1001/jama.2016.17216>
37. A. Esteva et al., Dermatologist-level classification of skin cancer with deep neural networks. *Nature* **542**, 115–118 (2017). <https://doi.org/10.1038/nature21056>
38. A.A.A. Setio et al., Pulmonary nodule detection in CT images: false positive reduction using multi-view convolutional networks. *IEEE Trans. Med. Imaging* **35**, 1160–1169 (2016). <https://doi.org/10.1109/TMI.2016.2536809>
39. Q. Dou et al., Automatic detection of cerebral microbleeds from MR images via 3D convolutional neural networks. *IEEE Trans. Med. Imaging* **35**, 1182–1195 (2016). <https://doi.org/10.1109/TMI.2016.2528129>